Application of Lattice Boltzmann Method for Simulation of Turbulent Diffusion from a CO_2 Lake in Deep Ocean

Jiang, Fei
Interdisciplinary Graduate School of Engineering Sciences, Kyushu University

Hu, Changhong
International Institute for Carbon-Neutral Energy Research (WPI-I2CNER), Kyushu University | Research Institute for Applied Mechanics, Kyushu University

出版情報：Journal of Novel Carbon Resource Sciences. 5, pp.10-18, 2012-02. Kyushu University G-COE program "Novel Carbon Resource Sciences" secretariat
バージョン：
権利関係：

Kyushu University Global COE Program
Journal of Novel Carbon Resource Sciences, Vol. 5, pp. 10-18, Feb. 2012

Application of Lattice Boltzmann Method for Simulation of Turbulent Diffusion from a CO_2 Lake in Deep Ocean

Fei Jiang[*1], Changhong Hu[*2,*3]

[*1]Interdisciplinary Graduate School of Engineering Sciences, Kyushu University
[*2]Research Institute for Applied Mechanics, Kyushu University
[*3]International Institute for Carbon-Neutral Energy Research (WPI- I2CNER), Kyushu University

(Received December 12, 2011; accepted January 19, 2012)

This paper presents a numerical method based on the Lattice Boltzmann (LB) scheme, which aims to accurately model and simulate the carbon dioxide (CO_2) dissolution, diffusion, and convection process in the condition of complex ocean current, turbulence and varying topography of the ocean floor. This LBM based scheme is carefully validated by using several benchmark test cases. A two-dimensional simulation study of CO_2 dissipation from a CO_2 lake is carried out to demonstrate the capability of the proposed method. The influence of the ocean current turbulence on the CO_2 dissolution rate is also discussed.

1. Introduction

The emission of greenhouse gases (GHG), such as carbon dioxide (CO_2), to the atmosphere is widely known to induce the global warming, and consequently changes the global climate system[1]. The ocean carbon capture and storage (CCS) technology has large potential for the mitigation of the global warming. Among the several ocean CCS strategies, considering that the liquid CO_2 is immiscible and relatively denser than seawater at depths greater than 3000 m, the ocean sequestration of CO_2 in the deep sea by forming a liquid CO_2 lake on the ocean floor attracts many scientists' attention. However the liquid CO_2 is expected to dissolve in the seawater. And the stability of the liquid CO_2 lake remains unclear, especially under the circumstance of complex ocean currents and varying topography of the ocean floor. The rate of dissolution is amplified under the conditions of ocean turbulence. Therefore, it is also very important to analyze the dissolution and diffusion behavior of the CO_2 to investigate the effects on the ecological environment of deep ocean. Because experiments in the deep ocean usually encounter difficulties such as riskiness and high cost, numerical simulation is considered to be an effective method. Fer and Haugan[2] attempt to envisage the fate of the liquid CO_2 lake through numerically solving the two-dimensional (2D) advection-diffusion equation. They investigated the effects of the bottom boundary dynamics and stratification above the hydrate layer on the CO_2 lake, however, the geometric property of the ocean bottom has not been taken into account. Kobayashi[3] developed a finite difference scheme using the boundary-fitted system to simulate the diffusion of CO_2 from the complicated geometric sea bottom basin. However, due to the coarse grid size, the results are lack of accuracy.

In this paper, we adopt a Lattice Boltzmann Method (LBM) for accurate modeling and large scale simulation of the CO_2 dissolution, diffusion, and convection process. The LBM provides an alternative way to solve fluid flow. Unlike the traditional CFD methods, which solve the conservation equations of macroscopic properties (i.e., mass, momentum, and energy) numerically, the basic idea of LBM is that it considers a many fictive particle system obeying the same conservation laws. Those particles perform consecutive propagation and collision processes over a discrete lattice mesh. LBM has several advantages over the conventional Navier-Stokes solver, especially in dealing with complex boundaries, incorporating of microscopic interactions, and parallelization of the algorithm. Further, as it is not necessary to solve the Poisson equation for pressure, the LBM is very efficient and suitable for large-scale parallel computing. All these features are required for accurate prediction of the CO_2 dissipation from a CO_2 lake in the deep sea. Therefore, the application of LBM makes it possible to achieve a high-resolution simulation for CO_2 dissipation that has not been realized before. In this paper, firstly, the details of the LBM are described. Then a couple of benchmark simulations including cavity turbulence flow and natural convection flow are conducted to validate the accuracy of LBM. And a two-dimensional simulation of CO_2 dissipation from a CO_2 lake is carried out to demonstrate and discuss the capability of the proposed method. Finally, the influence of the ocean current turbulence on the CO_2 dissolution rate is discussed.

2. Lattice Boltzmann method

Lattice Boltzmann method (LBM) is a mesoscopic kinetic-based approach that assumes the fluid flow to be composed of a collection of pseudo-particles which represented by a distribution function. Recently, because of its attractive simplicity of programming and capability of simulating complex fluid systems, LBM has rapidly emerged as a powerful technique with great potential for numerically solving momentum, energy, species transport and multi-phase problems[4]. In this study, we aim to use LBM to solve the diffusion and convection process of CO_2 in the deep ocean, which can be described

by the Navier-Stokes(NS) equations coupled with a convection-diffusion equation(CDE). In LBM, there are mainly two schemes for this kind of problem: the passive scalar approach and the hybrid approach. In hybrid approach, momentum conservation equations are solved by LB equation whereas the diffusion-advection equation for the scalar field is solved separately by using other conventional numerical techniques such as finite difference, finite volume or finite element method[5, 6]. However, it is very difficult to treat the complex boundary conditions by the hybrid approach. Therefore, in the present work, we choose the passive scalar scheme to solve the CDE. The standard LBGK(D2Q9) method based on a square lattice for solving the incompressible fluid flow are first briefly reviewed, and then a simple two dimensional four discrete velocities (D2Q4) LBGK model for scalar field is introduced for solving the CO_2 concentration distribution. Finally the two LBGK equations are coupled with each other by introducing a body force using the Boussinesq approximation.

2.1 The Lattice BGK equation for velocity field

The LBM model, a simplified fictitious molecular dynamic in which space, time, and particle velocities are all discrete, can be interpreted as the finite discrete velocity model of the Boltzmann equation. The occupations of the particles are represented by the single-particle distribution function $f_i(\mathbf{x},t)$, where i indicates the velocity direction. This function represents for the probability of finding a particle at node $\mathbf{x}$ and time t with velocity $\mathbf{c}_i$. In this study, the lattice BGK D2Q9 model (two dimensional, nine velocities) is adopted with discretized velocity vectors: $c_0(0,0)$, $c_1(1,0)$, $c_2(0,1)$, $c_3(-1,0)$, $c_4(0,-1)$, $c_5(1,1)$, $c_6(-1,1)$, $c_7(-1,-1)$, $c_8(1,-1)$. The collision operator of lattice Boltzmann equation is simplified by the single time relaxation approximation. Hence, the particle distribution function satisfies the following lattice Boltzmann BGK equation under the condition of low Mach number:

$$f_i(\mathbf{x}+\mathbf{c}_i\delta t, t+\delta t) - f_i(\mathbf{x},t) = \frac{1}{\tau}\left[f_i(\mathbf{x},t) - f_i^{eq}(\mathbf{x},t)\right] + F_i(\mathbf{x},t). \quad (1)$$

Here, f_i is the particle velocity distribution function, $\mathbf{c}_i$ is the particle velocity in the discretized direction. τ is the relaxation time, $F_i(\mathbf{x},t)$ is the forcing term added on the right-hand side of the LBE to reproduce the body force appearing in the NS equations which is given by equation (3), and $f_i^{eq}(\mathbf{x},t)$ is the local equilibrium distribution given as follow:

$$f_i^{eq}(\mathbf{x},t) = w_i\rho\left[1 + \frac{\mathbf{c}_i\cdot\mathbf{u}}{c_s^2} + \frac{(\mathbf{c}_i\cdot\mathbf{u})^2}{2c_s^4} - \frac{\mathbf{u}\cdot\mathbf{u}}{2c_s^2}\right], \quad (2)$$

$$F_i = w_i\frac{c_i\cdot\mathbf{F}}{c_s^2}, \quad (3)$$

where ρ is density, and $\mathbf{u}$ is the macroscopic velocity. And w_i is the weight factor corresponded to the particle velocity vector, which are given $w_0 = 4/9$, $w_1 \sim w_4 = 1/9$, and $w_5 \sim w_8 = 1/36$. $c_s = c/\sqrt{3}$ and $c = \delta x/\delta t$ is the ratio of lattice spacing δx and time step δt. And $\mathbf{F}$ is the body force in physical scale.

To derive this equilibrium distribution from the Maxwell distribution equation we must assure that the macroscopic characteristic velocity $\mathbf{u}$ is far smaller than the particle velocity $\mathbf{c}$, which can also be recognized as the incompressible condition for the particle evolution equation (1). The macroscopic properties density, velocity and pressure are defined in terms of particle distribution function by

$$\rho = \sum_{i=0}^{8} f_i, \quad \mathbf{u} = \frac{1}{\rho}\sum_{i=0}^{8} f_i\cdot\mathbf{c}_i, \quad P = \frac{\rho}{3}. \quad (4)$$

The relaxation time is related to the viscosity by

$$\nu = c_s(\tau - 0.5)\delta t. \quad (5)$$

After choosing an appropriate lattice size and the characteristic velocity for the LB system, we can calculate the viscosity above for a given Reynolds (*Re*) number. Consequently, the relaxation time is determined.

2.2 Lattice BGK equation for the scalar field

The scalar field is passively advected by the fluid flow and obeys a simple CDE

$$\frac{\partial T}{\partial t} + \nabla\cdot(uT) = D\nabla^2 T, \quad (6)$$

where D is the diffusivity and T is the scalar. Considering the memory consumption, we adopted a simple D2Q4 model for this scalar field. And a second particle distribution function T_i is introduced. Using lattice BGK model, the evolution of this scalar field for equation (6) is given by

$$T_i(\mathbf{x}+\mathbf{c}_i'\delta t, t+\delta t) - T_i(\mathbf{x},t) = \frac{1}{\tau'}\left[T_i(\mathbf{x},t) - T_i^{eq}(\mathbf{x},t)\right], \quad (7)$$

where τ' is dimensionless relaxation time, and T_i^{eq} is the local equilibrium value defined by

$$T_i^{eq}(\mathbf{x},t) = w_i T\left[1 + 2\mathbf{c}_i'\cdot\mathbf{u}\right]. \quad (8)$$

And discretized velocity vectors $\mathbf{c}_i'$ is defined by

$$\begin{bmatrix}\mathbf{c}_1' & \mathbf{c}_2' & \mathbf{c}_3' & \mathbf{c}_4'\end{bmatrix} = \begin{bmatrix}1 & -1 & 0 & 0\\ 0 & 0 & 1 & -1\end{bmatrix}. \quad (9)$$

Through the Chapman-Enskog procedure, we can determine the relationship between τ' and diffusivity D which is

$$D = \frac{2\tau' - 1}{4}\frac{\delta x^2}{\delta t}. \quad (10)$$

The macro scalar T is calculated from the scalar distribution function

$$T = \sum_{i=1}^{4} T_i. \quad (11)$$

2.3 Subgrid Turbulence Model

The simulation of CO_2 convection for the CSS problem requires considering a very large computation domain. It is necessary to introduce a turbulence model for such high Reynolds number problem. A simple route to the incorporation of turbulence modeling is to directly apply the concept of LES (Large Eddy Simulation) to the LB formulation. The LES aims at directly solving the large spatial-scale turbulent eddies that carry the majority of the energy, while modeling the smaller-scale eddies using a subgrid model. In this study, the unresolved scales is modeled by the widely used standard Smagorinsky model[7] that assumes the Reynolds stress term depends on the local strain rate tensor and leads to the eddy viscosity assumption. The eddy viscosity can be written as

$$\nu_t = (S_c \Delta)^2 \overline{S}, \qquad \overline{S} = \sqrt{2 S_j S_j}\,, \tag{12}$$

where S_c is the Smagorinsky constant (0.14 is used in this paper), Δ is the cutoff length scale set equal to the lattice-grid spacing. In LBM, the strain rate tensor given by $S_{ij} = 1/2(\partial_j u_i + \partial_i u_j)$, can be computed directly from the second-order moments $\widetilde{Q}$, of the non-equilibrium distribution function without direct finite differencing calculation of the velocity field.

Therefore, the characteristic value of the filtered strain rate tensor is given by

$$\overline{S} = \frac{\overline{Q}}{2\rho S_c \tau_{total}}, \tag{13}$$

in which $\overline{Q}$ is the filtered mean momentum flux computed from $\widetilde{Q}$:

$$\overline{Q} = \sqrt{2\sum_{i,j} \widetilde{Q}_{ij} \widetilde{Q}_{ij}}\,, \tag{14}$$

where $\widetilde{Q}$ can be simply computed by the filtered distribution functions at the lattice nodes:

$$\widetilde{Q}_{ij} = \sum_{k=1}^{8} c_{ki} c_{kj} (\bar{f}_k - \bar{f}_k^{eq}), \tag{15}$$

where c_{ki} is the kth component of the lattice velocity $\boldsymbol{c}_i$. The SGS approach is extremely convenient in terms of numerical implementations, because it leaves the LB equation unchanged except for the use of a new turbulent-related viscosity.

2.4 Boundary Condition

All the no-slip boundary condition for fluid field is handled by the half-way bounce back scheme[8]. This kind of modified bounce back scheme is of second-order spatial accuracy. The lattice distribution functions that will stream to no-slip boundary are reversed and then bounce back to the fluid field in the propagation process. Therefore this scheme is very suitable for the complex geometric boundary. For the Dirichlet boundary condition, a simple approach is to assign the equilibrium state to the distribution functions at a boundary node. Though some other kinds of schemes such as non-equilibrium extrapolation scheme were also tested, the equilibrium approach seems to be the most efficient and stable method to treat the given velocity boundary for the unsteady turbulent flow.

For a Neumann boundary condition of the scalar field, a similar scheme with the conventional way is adopted. First the macro-variable T is extrapolated, and then the equilibrium distribution can be assigned to the distribution functions at a boundary node. The flux boundary condition is necessary for the consideration of the CO_2 lake surface diffusion source in our simulation problem. The normal scalar flux j on the boundary is given by

$$j = \sum_{i=1}^{4} T_i c_i' \cdot n, \tag{16}$$

where n is the unit normal vector of the boundary surface. Therefore, for the bottom surface we can derive the flux boundary condition in LBM as:

$$T_3 = j + \sum_{i(c_i \cdot n \le 0)} T_i c_i' \cdot n. \tag{17}$$

3. Validation Work

3.1 Lid-driven Cavity Flow Simulation

In order to validate our method, the benchmark simulation of lid-driven cavity problem was first carried out. The problem considered is two-dimensional viscous flow in a cavity. An incompressible fluid is bounded by a square enclosure and the flow is driven by a uniform translation of the top. The physical space is divided into a regular square lattice with a domain size of 1024×1024 grids. As for the boundary condition, the top velocity boundary layer was set by applying the equilibrium function calculated from a constant velocity. And the simple bounce-back scheme for non-slip static walls was adopted. Two simulation cases with different Reynolds number (Re = 1000, 5000) were carried out first. The reference velocity of the top layer $\mathbf{u}_0$ is set to be 0.1. The corresponding relaxation parameters $1/\tau$, which can be derived from Eq(5), are 1.25(Re = 1000) and 1.7856(Re = 5000) respectively. We keep executing the computations until the behaviors of the flow became stable for each case. After the computation converged, the stream line contours for the cavity flow configurations with different Re numbers were shown in Figure 1. It is clear that there is one more vortex at the upper left side corner in the high Re number case. Ghia et al[9] have applied a multi-grid strategy and presented well-established results for the lid-driven cavity flow, whose work is the most comprehensive study of cavity flow to date. Comparisons between our results and Ghia's are shown in Figure 2(a) and Figure 2(b); **u** velocity profile is along the vertical centerline and **v** velocity profile is along the horizontal centerline of the cavity at steady state. The locations of primary and secondary vortices are presented in Table 1. It is obviously observed that all of our results showed excellent agreement with those given by Ghia[9].

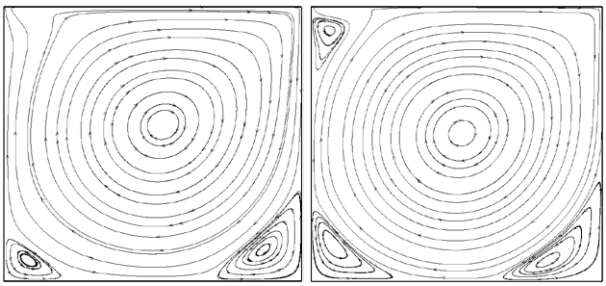

(a) *Re* = 1000 (b) *Re* = 5000

Fig. 1 Stream line contour of cavity flow.

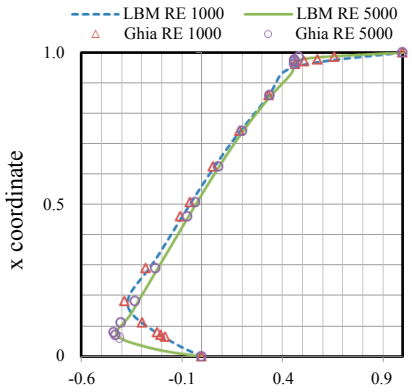

(a) **u** velocity profile

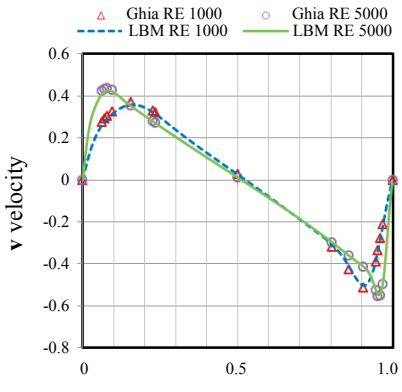

(b) **v** velocity profile

Fig. 2 Velocity profiles of the cavity at steady state.

Table 1 Location (x,y) of the primary and secondary vortices. (x_c,y_c): location of primary vortex; (x_{lr},y_{lr}): location of secondary vortex in the bottom corners.

Re	Method	x_c	y_c	x_l	y_l	x_r	y_r
10^3	LBM	0.5342	0.5626	0.0872	0.0775	0.8594	0.1094
	Ghia.U	0.5313	0.5626	0.0859	0.0781	0.8594	0.1094
5×10^3	LBM	0.5195	0.5352	0.0742	0.1328	0.8085	0.0743
	Ghia.U	0.5117	0.5352	0.0703	0.1367	0.8086	0.0742

3.2 Turbulent flow

As the validation of turbulence model, two cases (*Re* = 10^5 and *Re* = 10^7) were also carried out for the same lid-driven cavity problem. The computational conditions are exactly the same with the above validation work, and the SGS model for turbulence viscosity was incorporated into the LB formulation. The Smagorinsky number was set to be 0.14.

It is obviously seen that the scale of the vortices in the case of *Re* = 10^7 is much smaller. This consists with the turbulence theory (Figure 3). Compared with the results of NS-DNS method[10], both the pattern and the numbers of the vortex in our results show really good agreement. Therefore qualitatively speaking, the simulation results by this proposed LBM-LES method are accurate.

In addition, we have checked the flux term shown in Eq. (18) to verify that if it vanishes in the lid-driven cavity. We get a mean value in time around 3×10^{-4} by the LBM-LES method, while the DNS method[10] can achieve the precision of 6×10^{-5}.

$$\int_{\Omega} U \cdot (U \cdot \nabla) U dx dy \tag{18}$$

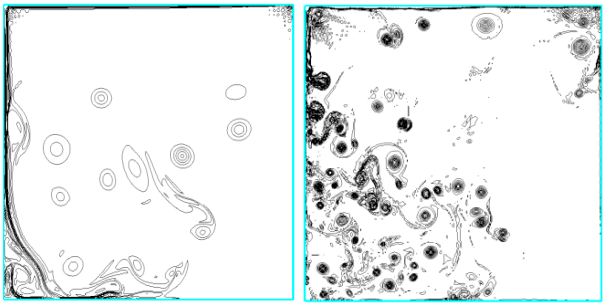

Fig. 3 Vorticity for *Re* = 10^5 (left) and 10^7 (right) at time step 200.

3.3 Validation of scalar field by natural convection flow

In order to verify the passive scalar LBGK model in our code, we carried out a benchmark simulation which is the natural convection in a 2D square cavity with two vertical side walls maintained at different temperatures. The temperature difference introduces a temperature gradient in a fluid, and consequently, the density difference induces a fluid convection motion. The other two walls are adiabatic. A lot of numerical solution works have been done related to this problem. De Vahl Davis[11] used a steam function vorticity finite difference method to obtain accurate benchmark solution for the natural convection in a square cavity. Using a finite volume multi-grid method, Hortmann et al[12] also obtained some reasonable results. This problem is governed by a dimensionless form of Boussinesq equations. In the Boussinesq approximation, the fluid temperature interaction is represented by a linear buoyancy term which acts as a body force on the fluid. The buoyancy term is assumed to depend linearly on the temperature

and is given by

$$G = \alpha g_0 (T - T_m)\vec{k}, \tag{19}$$

where α is the thermal expansion coefficient, g_0 is the acceleration due to gravity, $T_m = (T_L + T_H)/2$ is the average temperature, $\vec{k}$ is the vertical direction opposite to that of gravity.

The behavior of the flow is controlled by two dimensionless parameters: Rayleigh number *Ra* and Prandtl number Pr which are defined by

$$Pr = \frac{\upsilon}{D}, \quad Ra = \frac{g_0 \alpha \Delta T l_0^2}{\upsilon D}, \tag{20}$$

where l_0 is the reference length scale set to be the height of the cavity in this study, and $\Delta T = (T_H - T_L)$ is the temperature difference between the hot and cool walls. In the present validation work, LBM simulations were performed on a 1024×1024 uniform lattice with $Ra = 10^5$ and 10^6. In all simulations, *Pr* is set to be 0.71(air). The relaxation parameters are determined from the Prandtl and Rayleigh numbers. The non-slip boundary condition for velocity field is imposed on the four walls of the cavity. For the temperature boundary conditions, simple bounce back scheme is adopted for the horizontal walls. The Dirichlet boundary conditions are applied to the vertical walls.

The streamlines predicted for flows at two different Rayleigh numbers are shown in Figure 4. In $Ra = 10^5$ case there are two vortices near the center, while in $Ra = 10^6$ case, the two vortices move to take place near the walls and a third vortex appears in the core of the cavity. All these observations are in good agreement with the results reported in the previous studies[11, 12]

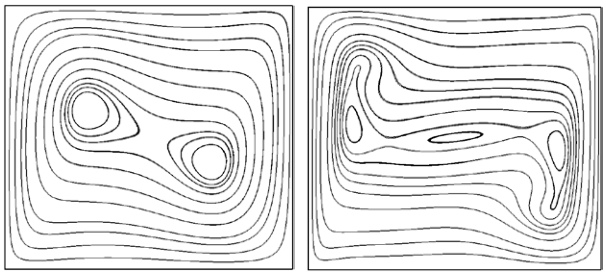

(a) $Ra=10^5$ (b) $Ra=10^6$

Fig. 4 Stream lines of the natural convection flow.

Some quantitative comparison of our LBGK results and the previous work are listed in Table 2. The comparison includes the average Nusselt number along the hot wall, the maximum horizontal velocity $\mathbf{u}_{max}$ obtained at y = 0.5, the maximum vertical velocity $\mathbf{v}_{max}$ obtained at x = 0.5 and the maximum value of the stream function ψ_{max} on the whole domain. The stream function is determined from

$$\nabla^2 \psi(x, y) = \frac{\partial v}{\partial x} - \frac{\partial u}{\partial y}. \tag{21}$$

The Nusselt number *Nu* is the major control parameter of the thermal transfer enhancement, which is defined by

$$Nu = -\frac{1}{T_H - T_L} \int_0^H \left(\frac{\partial T}{\partial x}\right)_{wall} dy. \tag{22}$$

As shown in Table 2, it can be found that our results also show good agreement with those of the other solutions, which indicates that the present method is able to simulate the coupling coefficient of the flow with a scalar field.

Table 2 Comparison of between our results and other studies.

Ra	Method	*Nu*	$\mathbf{u}_{max}$	$\mathbf{v}_{max}$	ψ_{max}
10^5	Davis[11]	4.509	34.730	68.590	9.612
	Hortmann[12]	4.521	34.740	68.639	No data
	Our results	4.535	34.841	68.267	9.623
10^6	Davis[11]	8.831	64.630	219.360	16.750
	Hortmann[12]	8.825	64.837	220.491	No data
	Our results	8.651	65.132	217.652	16.523

4. Simulation of CO_2 diffusion in the deep ocean

In order to simulate the CO_2 diffusion and convection process, the CO_2 concentration was considered as a scalar field and coupled with the flow field using the described LBM scheme above.

We consider a real scale two-dimensional geometry as shown in Figure 5, in which the width of CO_2 lake is 200 m. The whole x-direction domain is about 1Km. The ocean current is flowing from left to right side. In present study, the CO_2 lake surface is treated as a diffusion source, the diffusion coefficient in the CDE is adopted using the molecular diffusion coefficient of CO_2 *D*. This coefficient *D* is related to the temperature and the pressure, therefore considering the conditions of deep ocean, we evaluated the molecular diffusion coefficient to be 1.0×10^{-9} m^2/s according to the literatures[13, 14].

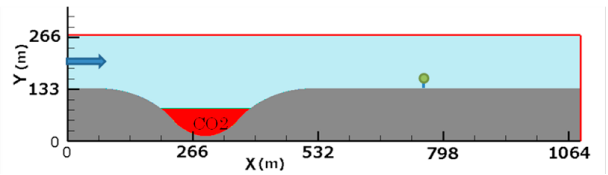

Fig. 5 2D domain of the simulation model.

For simplicity, the liquid CO_2 phase was not considered. It is known that the CO_2 hydrate forms an ice-like solid film at the interface between liquid CO_2 and seawater because of the high-pressure and low temperature conditions in the deep ocean. The transfer flux of CO_2 from the liquid CO_2 lake surface to the seawater is considered to be influenced by the mass transfer coefficient and the hydrate film thickness. The molar flux of liquid CO_2 into the water, J_{co_2}, can be written as

$$J_{co2} = \frac{1}{1-C_s}\left[K_m \frac{\rho_{mix}}{M_{mix}}(C_s - C_{amb}) - \frac{C_s}{1-C_s}J_w\right], \quad (23)$$

where M_{mix} and ρ_{mix} are the effective molar mass and the density of CO_2 saturated respectively. C_s is the solubility of CO_2 in seawater as mole fraction which is set to be 0.021[15]. C_{amb} is the ambient concentration around the hydrate. K_m is the mass transfer coefficient given by

$$K_m = 0.1 u_* Sc^{-0.67}, \quad (24)$$

in which u_* is the friction velocity which can be calculated by $u_* = u_{average}/30$, and $Sc = \upsilon / D$ is the Schmidt number and D is the molecular diffusivity of CO_2 in seawater. M_{mix} is defined as

$$M_{mix} = M_w(1-C_s) + M_{CO_2}C_s, \quad (25)$$

where molar mass of seawater M_w can be estimated as 0.023 kg/mol and the molar mass of CO_2 M_{CO_2} is set to be 0.044 kg/mol. The flux of water through the hydrate film J_w can be calculated as

$$J_w = \frac{r_c}{\tau^2}\frac{\gamma\cos\phi}{4\delta M_{mix}\upsilon_{mix}}(1-C_s), \quad (26)$$

where υ_{mix} is the kinematic viscosity of seawater saturated with CO_2, and δ is the hydrate-film thickness given by

$$\delta = \frac{r_c p}{\tau^2}\frac{\gamma\cos\phi}{4\eta_{mix} n K_m}\frac{(1-C_s)^2 + nC_s^2}{C_s - C_{amb}}, \quad (27)$$

in which r_c is the capillary radius, p is the porosity of the hydrate film, γ is the liquid CO_2-water interfacial tension, τ is the tortuosity of the capillaries, ϕ is the water side contact angle on the capillary wall, η_{mix} is the viscosity of seawater saturated with CO_2, and n is the hydration number. Using the parameter values presented in Table 3, finally we got the value of flux J_{co_2} to be 1.53×10^{-5} kg/(s×m^2) considering that C_{amb} is negligible compared to C_s.

Table 3 Parameters used for the calculation of CO_2 flux.

Parameter	$r_c(m)$	p	$\gamma(N/m)$	$\eta_{mix}(pas)$	ϕ
Value	10^{-8}	10^{-3}	19.4×10^{-3}	1.48×10^{-3}	0°
Parameter	τ	n	$\upsilon_{mix}(m^2/s)$	$\rho_{mix}(kg/m^3)$	M_{mix}
Value	2	5.75	1.3×10^{-6}	1041	0.023

In terms of the computation conditions, the whole computation domain is divided into uniform square lattices with grid size 8192×2048. The computation was carried out on a conventional workstation platform with an Intel Xeon X5680 (3.33GHz) CPU and an Nvidia Tesla C2050 GPU (Graphics Processing Unit) equipped. The computation time is about one day with the application of parallel GPU computing technology. The Reynolds number is calculated using the characteristic length of the CO_2 lake and the ocean flow velocity. In present study, we chose two conditions: a normal ocean current velocity 0.02 m/s and another velocity 0.2 m/s under the benthic storm condition (episodic events of strong, bottom-intensified currents), which lead to the *Re* number to be 2.5×10^6 and 2.5×10^7, respectively. Non-slip condition is adopted at the sea bottom for both velocity and scalar field. A uniform velocity $\mathbf{u}_0$, as a Dirichlet condition, is applied at the inflow, outflow and the upper side of the domain for the flow field, while for the concentration scalar field, the Neumann condition is used at the same place. The flux boundary condition is adopted for the diffusion source at the CO_2 lake surface. The computations are kept running until the flow passed the CO_2 lake for over 15 hours.

We focus the results at the time after the ocean currents occurred for 14 hours above the CO_2 lake. The stream lines of the velocity field at the left corner of the CO_2 lake are shown in Figure 6. It is obvious that the eddy phenomenon is significant in both two cases due to the extremely high Reynolds number; and the flow is in an unsteady turbulent state.

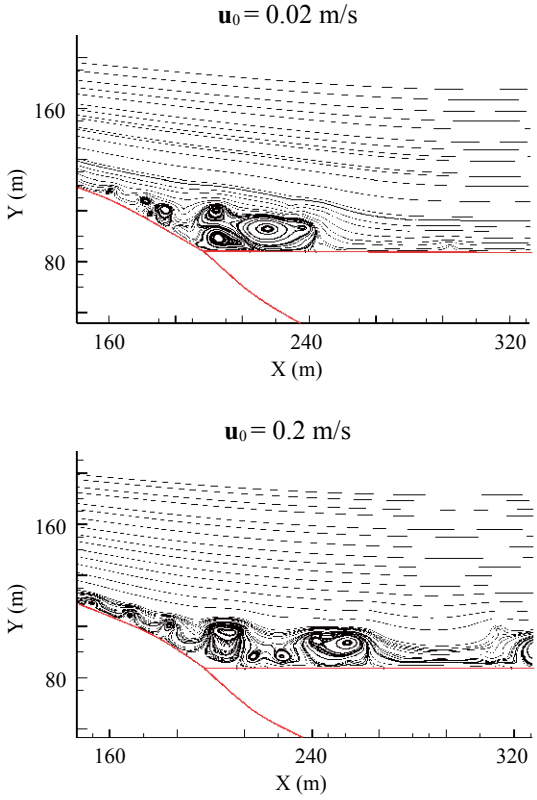

Fig. 6 Stream line of the velocity field in the left corner at time 14 hour.

The normalized horizontal direction velocity profiles at the center of the basin above the CO_2 lake at a certain time step are presented in Figure 7(a). The large fluctuation of velocity appeared in the high Reynolds number case. Since, under the turbulent circumstance, the time averaged value is much more important than the value of a specific time point, therefore, the values of x-direction velocity above the lake surface were averaged from 10 to 15 hour when the flow field has already reached a semi-steady status. The averaged results are shown in Figure 7(b). And it can be found that the turbulent boundary layer in the high Reynolds number case is thinner than that in the low Reynolds number case, which is reasonable in turbulence theory.

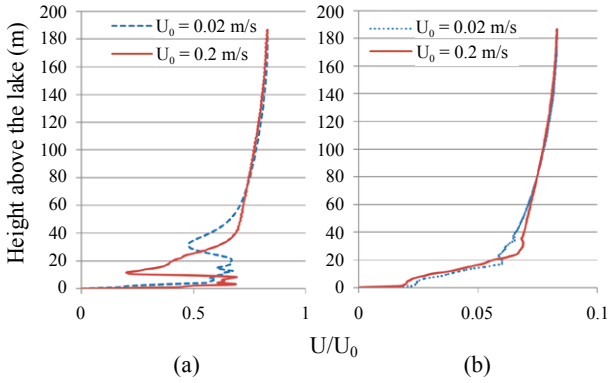

Fig. 7 (a) Normalized X direction velocity profiles at the center of the basin above the CO_2 lake at time 12 hour.
(b) Averaged value of normalized X direction velocity profiles from 10 to 15 hour.

The results of CO_2 concentration distribution above the lake are shown in Figure 8. Since the molecular diffusion coefficient of CO_2 is in an order of 10^{-9}, the Péclet number defined as

$$Pe = \frac{Lu}{D}, \tag{28}$$

is very large. L and u are the characteristic length and velocity respectively. As a result the convection term plays a primary role in the whole computation. Consequently, the behavior of the CO_2 dispersion is mainly controlled by the turbulence flow. It is obviously revealed that thickness of the stratified CO_2 concentration layer in low current velocity case is larger than that in high current velocity case. The reason is that the CO_2 density layer is supposed to be flushed away by the high-speed flow in the benthic storm conditions.

In addition, the CO_2 concentration on the vertical direction at the center of the basin above the CO_2 lake was averaged from 10 to 15 hour to figure out the detailed information of the CO_2 stratified layer for the two different cases (Figure 9). It is clear that the stratified CO_2 concentrated layer in low velocity case is about 6m, while in high velocity case the thickness is only 1m. Therefore we can get the conclusion that under the normal ocean flow condition the CO_2 lake is relatively stable, however when the ocean storm comes, the stratified CO_2 density layer may become less stable due to the strong turbulence flow. Consequently, more CO_2 will be dissolved into seawater due to the weaken suppression effect of the stratified layer. The hydrate membrane is also in danger of disruption by the sweep-past of eddies from the adjacent turbulent region, resulting in a higher dissolution rate of the CO_2.

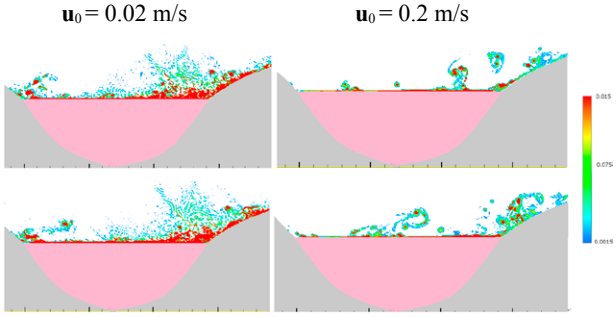

Fig. 8 Contour of the CO_2 concentration at time 9 hour (up) and 9.2 hour (down) for the two different velocity cases.

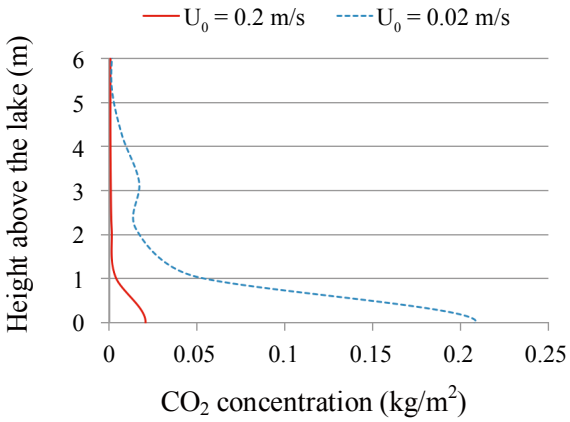

Fig. 9 Vertical profiles of the averaged CO_2 concentration from 10 to 15 hour at the center of the basin above the CO_2 lake.

Furthermore, we set an observation point with a distance about 500 m downside from the CO_2 lake center in order to investigate the CO_2 mass flux. The variations of the CO_2 mass flux with time at the observation point in the two different velocity cases are shown in Figure 10. After the flow reached a semi-steady state, the CO_2 flux is fluctuating greatly in both two cases due to the turbulent flow. The CO_2 diffuses from the source to the observation point much faster when the benthic storm happens. It can be found in the Figure 10 that the CO_2 substance appeared at the observation location after the benthic storm occurred for only about 1 hour, while in the normal speed flow condition it takes over 10 hours for the CO_2 to reach the observation point.

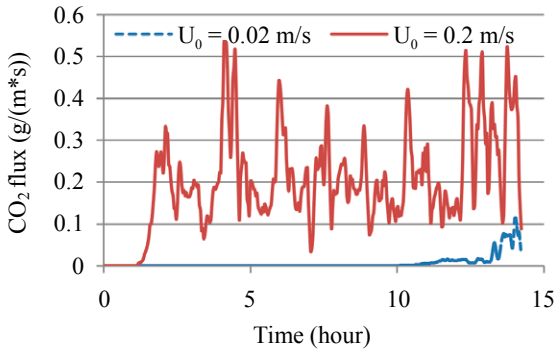

Fig. 10 CO_2 mass flux at the observation point.

On the other hand, under the benthic storm circumstance, the magnitude of CO_2 mass flux is much larger than that in the normal status. The CO_2 flux reaches about an average value of 0.28 g/(m×s) in the $\mathbf{u}_0$ = 0.2 m/s case, while in the normal speed $\mathbf{u}_0$ = 0.02 m/s case, the average of the CO_2 flux is only around 0.034 g/(m×s). In addition, we integrated the mass of CO_2 across the observation surface. As shown in Figure 11, the detail information of the quantity of the CO_2 that flow over a certain section can be checked at any time. In our demonstration case, after the flow occurred for 14 hours, the CO_2 quantity across the observation place reached over 200 kg in the high velocity case, and only 7 kg in the low velocity case. It is possible to predict that the relationship between diffused CO_2 quantity and time is nearly linear (Figure 11). Therefore, we can estimate the time of complete dissolution for a certain CO_2 lake. We assume that CO_2 lake in our case has a surface area of 200×200 m^2 and an initial depth of 50m. The total amount of liquid CO_2 in the lake is 2.096×10^6 ton, using density of liquid CO_2~1050 kg/m^3, which corresponds to one year of emission from a 400 MW coal-fired power plant. Under the high velocity condition, it takes only 16.8 years for the complete dissolution of CO_2, while under the normal low velocity condition of flow the CO_2 lake can be reserved for about 478 years which is a considerable period for the mitigation of global warming.

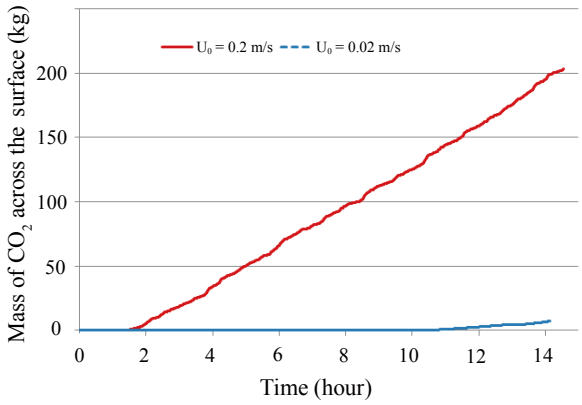

Fig. 11 Integral of CO_2 mass flux at the observation surface.

The fast ocean flow speed lead to the high CO_2 dissolution rate and consequently caused corresponding large quantity of CO_2 mass flux. Therefore, benthic storm is still considered to be a terrible condition for the CO_2 ocean sequestration as a liquid pool. And the benthic storm occurred about four times a year with duration of about one week. Therefore, the feasibility of CO_2 ocean sequestration needs some further research and evaluation.

According to the above results, we investigated the detail effect of the different ocean flow speed for the stratified CO_2 layer formation, the CO_2 mass flux at the downside observation place and the complete CO_2 dissolution time. The results indicate that the high velocity of the flow in a benthic storm condition may cause some bad influence to the stability of the CO_2 lake due to the decreasing of the density layer above the lake surface. As a result, the increase of the CO_2 mass flux in downside of the flow may cause some damage to the ecosystem in the deep ocean. However, under the normal ocean flow conditions, the CO_2 lake is relatively stable and can be preserved for a considerable time.

Obviously, our LBM based CFD method is proved to be able to provide much more detail information including the flow velocity field under complex topography and the CO_2 concentration variation at any location. Therefore, accurate evaluation related to CCS can be made based on the data of our simulation.

5. Conclusion

In this paper, we have proposed a LBM method for the large-scale simulations of CO_2 diffusion and convection in the deep ocean.

At first, validation of the method has been done against some benchmark examples. Computational accuracy of the turbulent flow solver and the passive scalar model has been carefully checked. Then this method has been extended for modeling CO_2 dispersion from a CO_2 lake, with the consideration of the effect of the CO_2 hydrate which covers the CO_2 lake. We investigated two cases with different ocean flow speeds. The results show that for the high velocity case which is corresponding to the benthic storm condition, density stratification above the CO_2 hydrate are swept away by the strong current, resulting in high dissolution rate of the CO_2. On the other hand, for the normal velocity case, the CO_2 lake is relatively stable.

Our method is demonstrated to be very powerful for simulation of the CO_2 dispersion problem which can provide much more detailed information including the flow velocity field under complex circumstances and the CO_2 concentration variation at any location. Furthermore, this LBM approach is very suitable for parallel computation, implementation of it for multi-GPU computing will been done in the future work.

Acknowledgements: This work was supported in part by World Premier International Research Center Initiative (WPI), MEXT, Japan.

References

1) J. T. Houghton, L. G. M. Filho, J. Bruce, H. Lee, B. A. Callander, E. Haites, N. Harris and K. Maskell, *Climate change, 1994 : radiative forcing of climate change and an evaluation of the IPCC IS92 emission scenarios*, Cambridge University Press, Cambridge (1995).
2) I. Fer and P. M. Haugan, *Limnology and Oceanography*, **48**(2), 872 (2003).
3) Y. Kobayashi, *The Japan Society of Naval Architects and Ocean Engineers*, **106**, 19 (2003).
4) S. Chen and G. D. Doolen, *Annual Review of Fluid Mechanics*, **30**, 329 (1998).
5) P. Lallemand and L.-S. Luo, *Physical Review E*, **68**(3), 036706 (2003).
6) P. Lallemand and L.-S. Luo, *International Journal of Modern Physics B*, **17**(1/2), 41 (2003).
7) J. Smagorinsky, *Mon. Wea. Rev.*, **91**, 99 (1963).
8) X. Y. He, Q. S. Zou, L. S. Luo and M. Dembo, *J. Stat. Phys.*, **87**, 115 (1997).
9) U. Ghia, K. N. Ghia and C. T. Shin, *Journal of Computational Physics*, **43**, 387 (1982).
10) Ch.-H. Bruneau, M. Saad, *Computational Fluids Dynamics Journal*, **15**(3) (2006).
11) G. De Vahl Davis, *International Journal for Numerical Methods in Fluidse*, **3**(3), 249 (1983).
12) M. Hortmann, M. Perić, G. Scheuerer, *International Journal for Numerical Methods in Fluids*, **11**, 189 (1990).
13) C. R. Wilke and P. Chang, *AIChE J.*, **1**, 263 (1955).
14) T. K. Sherwood, R. L. Plgford, C. R. Wilke, *Mass Transfer*, McGraw Hill, New York (1975).
15) I. Aya, K. Yamane and H. Nariai, *Energy*, **22**, 263 (1997).
16) Y. Shi, T. S. Zhao and Z. L. Guo, *Physical Review E*, **70**, 066310 (2004).